Multifunctional soft stretchable strain sensor for complementary optical and electrical sensing of fatigue cracks

OPEN ACCESS
IOP Publishing
Smart Materials and Structures
Smart Mater. Struct. **32** (2023) 045010 (15pp)
https://doi.org/10.1088/1361-665X/acbef2

Multifunctional soft stretchable strain sensor for complementary optical and electrical sensing of fatigue cracks

Han Liu[1,*], Matthias Kollosche[2], Simon Laflamme[1,3] and David R Clarke[2]

[1] Department of Civil, Construction, and Environmental Engineering, Iowa State University, Ames, IA 50010, United States of America
[2] Harvard John A. Paulson School of Engineering and Applied Sciences, Harvard University, Cambridge, MA 02138, United States of America
[3] Department of Electrical and Computer Engineering, Iowa State University, Ames, IA 50010, United States of America

E-mail: liuhan@iastate.edu

Received 12 October 2022, revised 9 February 2023
Accepted for publication 24 February 2023
Published 8 March 2023

Abstract

Fatigue-induced cracking in steel components and other brittle materials of civil structures is one of the primary mechanisms of degrading structural integrity and can lead to sudden failures. However, these cracks are often difficult to detect during visual inspections, and off-the-shelf sensing technologies can generally only be used to monitor already identified cracks because of their spatial localization. A solution is to leverage advances in large area electronics to cover large surfaces with skin-type sensors. Here, the authors propose an elastic and stretchable multifunctional skin sensor that combines optical and capacitive sensing properties. The multifunctional sensor consists of a soft stretchable structural color film sandwiched between transparent carbon nanotube electrodes to form a parallel plate capacitor. The resulting device exhibits a reversible and repeatable structural color change from light blue to deep blue with an angle-independent property, as well as a measurable change in capacitance, under external mechanical strain. The optical function is passive and engineered to visually assist in localizing fatigue cracks, and the electrical function is added to send timely warnings to infrastructure operators. The performance of the device is characterized in a free-standing configuration and further extended to a fatigue crack monitoring application. A correlation coefficient-based image processing method is developed to quantify the strain measured by the optical color response. Results show that the sensor performs well in detecting and quantifying fatigue cracks using both the color and capacitive signals. In particular, the color signal can be measured with inexpensive cameras, and the electrical signal yields good linearity, resolution, and accuracy. Tests conducted on two steel specimens demonstrate a minimum detectable crack length of 0.84 mm.

* Author to whom any correspondence should be addressed.

Keywords: optical, structural color, capacitor, fatigue crack, strain sensing, carbon nanotubes, structural health monitoring

(Some figures may appear in colour only in the online journal)

1. Introduction

Fatigue cracks in steel are damages that can lead to sudden and catastrophic failures of structural components and/or the structure itself [1, 2]. Currently, these cracks are identified visually during inspection campaigns [3]. In some cases, they may also be identified and characterized using nondestructive evaluation (NDE) techniques, such as magnetic particle testing [4], ultrasonic testing [5], thermography [6]. Nevertheless, visual inspections do not guarantee the timely discovery of new cracks, because the process is subjective and also conducted at pre-determined time intervals [3]. NDE techniques are costly, time consuming, and require trained agents.

Timely discovery of damage can be achieved using structural health monitoring (SHM) technologies. Electromechanical methods are popular SHM techniques used to detect cracks through local changes in electrical properties. For example, using restive paints [7], carbon nanotube (CNT)-based films [8, 9], flexible sheets of resistors [10], and soft elastomeric capacitors [11]. The promise of these technologies lies in the coverage of large structural surfaces enabling both fatigue crack discovery and quantification during operations. In particular, the authors have investigated multiple designs of capacitive strain sensors that allow for processing and design of a soft elastomeric sensing skin that can conduct two-dimensional (2D) sensing of strain. This 2D sensing property was leveraged to create a sensing solution capable of discovering new fatigue cracks on flat surfaces [11] and in corner welds [12]. The research presented on this paper builds on experience with these soft elastomeric sensing skins.

Alternative SHM methods have also been proposed, in particular those based on change in optical properties. Optical properties can be leveraged to assist in damage detection and visualization during visual inspections. Investigations on structurally colored materials that undergo visible (400–800 nm) absorption and spectral emission changes in response to external stimulus have been conducted and reported over the last decades [13, 14]. Structurally colored materials that response to mechanical stimuli have been proposed for optical sensing [15]. The promise of that materials is that color change or intensity change can be obtained without degradation under external mechanical stimuli. However, maintaining structural film integrity over large, reversible strains still remains challenging [16], and other color-dynamic materials such as liquid crystalline elastomers are difficult to scale up and be transformed into optical sensors [17]. To that effect, polymer-based structurally colored materials capable of changing color or emission color without degradation upon external mechanical stimuli have been proposed [18, 19].

Examples of optical sensing applications to civil engineering, (GNP)-based polymer composite fabricated by performing *in situ* GNP reduction directly within the elastomeric poly(dimethyl siloxane) (PDMS) matrix for large strain sensing via visual observation [20], an opal photonic crystal film made of a silicone elastomer with arrays of submicron polystyrene colloidal particles to detect cracks on concrete [21], a mechanoresponsive sensor formed by a PDMS substrate and polystyrene–polybutadiene–polystyrene (SBS) triblock copolymer film to detect mechanical deformations in metallic structures [22], and an angle-insensitive mechanoresponsive sensor formed by sandwiching an Fabry–Perot (F–P) interferometer composed of an elastomeric triblock copolymer between two metal layers to detect mechanical failure of material [23]. These polymer-based mechanoresponsive soft photonic materials are promising at reducing the subjectivity of visual inspections, yet do not guarantee timely discovery of damage.

Here, we describe a new multifunctional skin sensor technology that combines both optical and electrical responses to strain. The novelties of the paper are twofold: (1) the optical signal of the structural color film is angle-independent and thus greatly facilitates field measurements using an affordable camera; and (2) the optical and capacitive signals are combined to improve the detection and identification of fatigue cracks. The purpose of the optical signal is to visually assist in locating fatigue cracks, and that of the capacitive signal is to send timely warnings to infrastructure operators. The optical function does not rely on power and is engineered to visually assist the localization of fatigue cracks. The capacitance sensing function does require a data acquisition and transmission system, and is added to send timely warnings to infrastructure operators. The optical property arises from a structural color film, fabricated with monodispersed silica nanoparticles (NanoCym). Its mechanoresponsive behavior results in a reversible, observable to the naked eye, and angle-independent color change under an ambient environment. This color film is then sandwiched between two transparent CNT electrodes to produce a flexible, parallel plate capacitor to add the electromechanical property. The soft capacitor is capable of transducing strain into a measurable change in capacitance. The purpose of the CNT electrodes is to minimize the optical impact on the optical properties.

The optical and electromechanical sensing properties are characterized and evaluated through tensile tests and fatigue crack tests on steel plates (compact tension (C(T)) specimens). A correlation coefficient-based image processing method is developed to quantify strain caused by the opening of the fatigue crack from the optical response. This algorithm allows for an easy vision-based crack detection and quantification method, and does not require a high-resolution camera.

The rest of the paper is organized as follows. Section 2 provides the background of the technology, including the

fabrication process, electromechanical model, and structural similarity index measurement (SSIM) for image processing. Section 3 describes the experimental setup and procedure applied for the free-standing and fatigue crack tests. Section 4 characterizes mechanical, optical, and electromechanical properties. Section 5 presents and discusses results on the sensing performance. Section 6 concludes the paper.

2. Multifunctional sensor

This section presents the multifunctional sensor for SHM of fatigue cracks. It includes the fabrication process of the structural color film and the parallel plate capacitor structure, the electromechanical model, and the SSIM used for image processing and strain measurement.

2.1. Structural color film

The fabrication steps of the soft structural color film are illustrated in figure 1(a). The silica nano-articles with a diameter of 100 nm are purchased from NanoCym and washed in anhydrous ethanol at least three times. After, the particles are dispersed in anhydrous ethanol in a ratio of 1:10 w/w. The host polymer matrix poly(ethylene glycol) phenyl ether acrylate (Sigma-Aldrich) is mixed with 1 w/w of photoinitiator (2-hydroxy-2-methyl-1-phenyl-1-propanone, Sigma-Aldrich), named monomer. The silica particles and the matrices in a ratio of 40 wt% of SiO_2 are mixed using a shear mixer for 5 min at 2000 rpm, and the resulting composite is stored at 70 °C to evaporate the ethanol for several hours. The resulting material is cast onto glass slides. To enable easy peeling of the stretchable composite, a sacrificial layer of water-soluble dextran (MW 15 000–25 000, Sigma Aldrich) was first spin coated onto the glass slide. In a final step, the composite was cured under UV light and nitrogen atmosphere for 5 min at 8 W and 254 nm wavelength for solidifying.

The structural color relies upon the interference of light, scattered in the nanoscale structures of randomly arranged silica spheres. Different materials hosting nanostructure can be employed, among them polymers or other responsive materials. The mechanical properties provided by the polymer matrix allows to use external triggers such as strain, temperature, and change in the scattering structure, to producing changes in the optical appearance. This enables tuning and therefore added functionalities of materials for different applications such as sensors, displays, and camouflage. The essential characteristic of our structural color film is the stretchability of the soft composite and a predictable and reversible color response to an external stimuli. In this study, silica (SiO_2) particles were employed to serve as photonic structure changes in their density, enabling a reversible, repeatable, and angle-independent color changes under stretch. The optical functionality can be used to recognize the presence of fatigue cracks on steel given the strain provoked by the opening of the crack, as illustrated in figure 1(c).

2.2. Parallel-plate capacitor

When electroded on both sides, the silica/elastomer composite film becomes a parallel plate capacitor as shown in figure 1(b). The electrodes on the structural color composite film are defined by a masking layer applied directly after peeling of the cured polymer film. To form a stretchable fairly transparent electrode, CNT electrodes are prepared from a commercially available CNT solution (Invision 3500, NanoC). An amount of 5 ml CNT ink is diluted in isopropanol, sonicated for 10 min and vacuum filtered through a porous polytetrafluoroethylene (PTFE) membrane with a pore size of 0.5 nm. The resulting PTFE filter membrane had a sheet resistance of 600 $\Omega\,\mathrm{Sq}^{-1}$ (20J3 Sheet Resistance Meter, DELCOM Instruments, Inc.). A masking layer was used to define the electrode areas, produced by stamping, on both sides of the film. The PTFE filters with the CNT electrode was stamp-transferred onto both sides of the prior prepared structural color film to define the parallel plate capacitor structure, simultaneously combining a optical and electrical sensing properties. In a final step, electrical connections were applied and the sensors transferred for testing and evaluation. The two electrodes are highly compliant and transparent, thus minimizing optical absorption. Consistency and uniformity of specimens is ensured through a quality control process that consists of measuring and evaluating the thickness, color response, permittivity, dissipation factor, and initial capacitance across the optical and electrical properties.

2.3. Electromechanical model

From prior experience on soft elastomeric capacitors, our sensor can be modeled as a parallel plate capacitor [24, 25]:

$$C = e_0 e_r \frac{A}{h} \tag{1}$$

where $e_0 = 8.854\,\mathrm{pF\,m^{-1}}$ is the vacuum permittivity, e_r is the relative permittivity, h is the thickness of the dielectric (color film), and $A = l \cdot d$ is the electrode area of length l and width d as annotated in figure 1(d).

Assuming that the sensor undergoes small levels of strain, the relative change in capacitance $\Delta C/C_0$ can be obtained by differentiating equation (1) and relates to the additive in-plane strains $\varepsilon_x = \Delta l/l_0$, $\varepsilon_y = \Delta w/w_0$, and out-of-plane strain $\varepsilon_z = \Delta h/h_0$:

$$\frac{\Delta C}{C_0} = \left(\frac{\Delta l}{l_0} + \frac{\Delta w}{w_0} - \frac{\Delta h}{h_0}\right) = \varepsilon_x + \varepsilon_y - \varepsilon_z \tag{2}$$

where C_0 denotes an initial (unstrained) condition, and ΔC represents the incremental change in capacitance. Taking the small and additive in-plane strain ($x-y$ plane) of a monitored substrate and applying Hooke's Law under plane stress assumption, one obtains:

$$\varepsilon_z = -\frac{\nu}{1-\nu}(\varepsilon_x + \varepsilon_y) \tag{3}$$

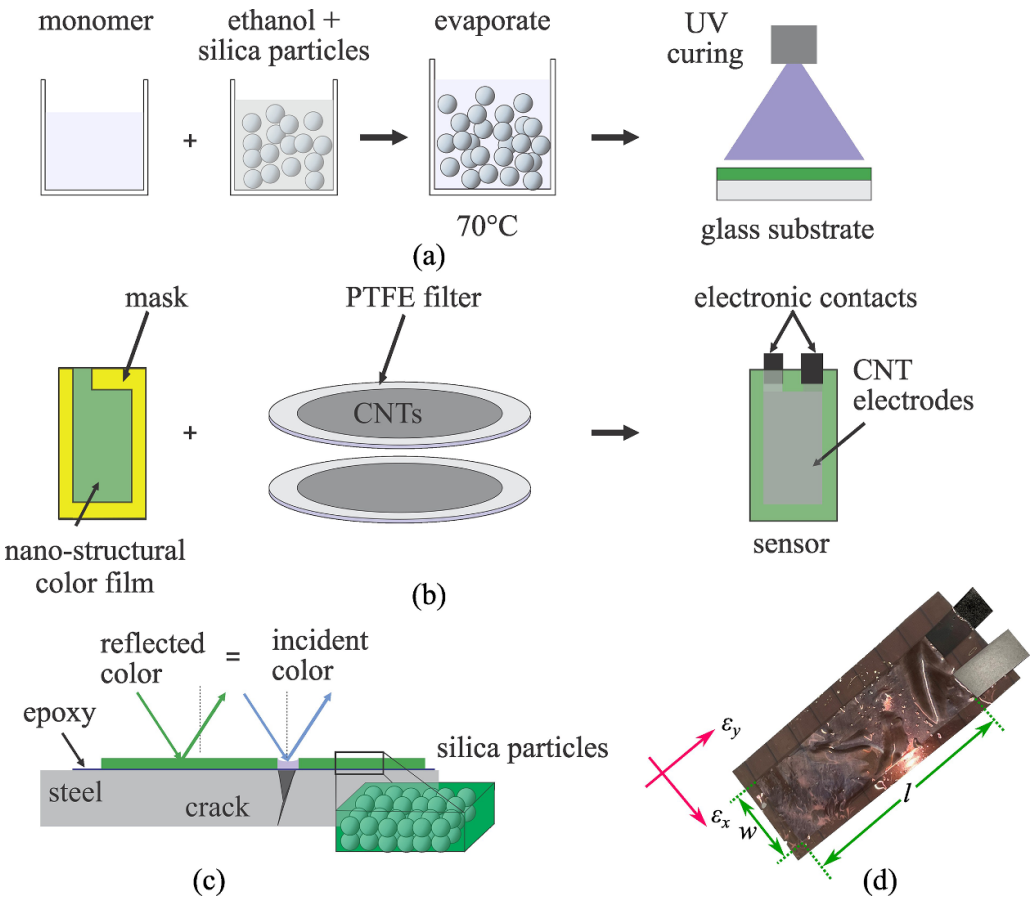

Figure 1. (a) Fabrication steps of the structural color film capacitor material; (b) formation of the CNT electrodes by CNT stamping; (c) optical mechanism; (d) and picture of the assembled sensor.

where ν is the Poisson's ratio of the structural color film. Substituting equation (3) into equation (2), the capacitance of the sensor under uniaxial strain (along the x-axis) can be written as:

$$\frac{\Delta C}{C_0} = \frac{1}{1-\nu}(\varepsilon_x + \varepsilon_y) = \lambda_0(\varepsilon_x + \varepsilon_y) \tag{4}$$

where λ_0 is the gauge factor in a free-standing (sensor not adhered onto a substrate) configuration. In an adhered configuration, the gauge factor λ is influenced by the level of adhesion, creating a composite effect [26], and the stiffness of the substrate. Therefore, equation (4) can be specialized with $\varepsilon_y = -\nu_c\varepsilon_x$, where ν_c is the resulting Poisson's ratio under composite action and can be expressed as a function of weighted Poisson's ratios:

$$\nu_c = \frac{a\nu + b\nu_m}{a+b} \tag{5}$$

where ν_m is the Poisson's ratio of the substrate, a and b are weight coefficients representing the composite effect with values between 0 and 1. Coefficients a and b depend on the level of adhesion and material stiffness, with $a+b=1$. For steel, concrete, and other structural materials of high stiffness, $a \approx 0$ and $b \approx 1$, and for free-standing sensors, $a=1$ and $b=0$. Substituting $\varepsilon_y = -\nu_c\varepsilon_x$ into equation (4), one obtains:

$$\frac{\Delta C}{C_0} = \frac{1-\nu_c}{1-\nu}\varepsilon_x = \frac{1-\frac{a\nu+b\nu_m}{a+b}}{1-\nu}\varepsilon_x \tag{6}$$

yielding the gauge factor λ:

$$\lambda = \frac{1-\nu_c}{1-\nu}. \tag{7}$$

2.4. Structural Similarity Index Measurement (SSIM)

The SSIM is a perceptual metric used to measure and quantify visual similarity between images [27, 28]. Mathematically, the SSIM is computed as the weighted combination of the luminance contrast, and structure similarity between two images p and q [29]:

$$\mathrm{SSIM}(p,q) = [k(p,q)]^{\alpha} \cdot [c(p,q)]^{\beta} \cdot [s(p,q)]^{\gamma} \tag{8}$$

where k is the luminance used to compare the brightness between both images, c is the contrast used to differ the ranges between the brightest and darkest region of both images, s is the structure used to compare the local luminance pattern to find the similarity and dissimilarity between both images, and

α, β, and γ are positive constants. The luminance, contrast, and structure of an image can be separately expressed as:

$$k(p,q) = \frac{2\mu_p\mu_q + C_1}{{\mu_p}^2 + {\mu_q}^2 + C_1} \tag{9}$$

$$c(p,q) = \frac{2\sigma_p\sigma_q + C_2}{{\sigma_p}^2 + {\sigma_q}^2 + C_2} \tag{10}$$

$$s(p,q) = \frac{\sigma_{pq} + C_3}{\sigma_p\sigma_q + C_3} \tag{11}$$

where μ_p and μ_q are the local mean of p and q, σ_p and σ_q are the standard deviations of p and q, and σ_{pq} is the cross-covariance for images p and q, respectively [30].

By substituting equations (9)–(11) into equation (8) and assigning $\alpha = \beta = \gamma = 1$, the SSIM can be is simplified as:

$$\mathrm{SSIM}(p,q) = \frac{(2\mu_p\mu_q + C_1)(2\sigma_p\sigma_q + C_2)}{({\mu_p}^2 + {\mu_q}^2 + C_1)({\sigma_p}^2 + {\sigma_q}^2 + C_2)}. \tag{12}$$

3. Experimental test

This section describes the experimental method used in characterizing the sensor. First, the quasi-static tests used to investigate the optical and electro-mechanical properties of the sensor under a free-standing configuration are described. Second, the experimental setup along with the loading protocol used in testing fatigue crack detection and quantification capabilities are presented.

3.1. Free-standing test

Quasi-static tests were designed to characterize the sensor under a free-standing configuration. Sensors were customized in rectangular-shaped thin-film specimens, each of 56 mm length, 8 mm width, and 0.15 mm thickness, for an aspect ratio of 7:1. Experimental tests were conducted using an Instron 5544A tensile tester equipped with a 10 N load cell (shown in figure 2(a)). Both ends of the sensor were gripped between two clamping fixtures and mounted onto the load cell. Three independent specimens were prepared and each were initially pre-strained at 50 mN to eliminate slack before testing.

A first series of tests was conducted by applying uniaxial tensile strain along the longitudinal direction at a linear rate of 1% s^{-1} and stopped at 40% strain. A second series of tests consisting of cyclic loadings was conducted by subjecting the sensor to a 0.1 Hz excitation at 0.5%, 1%, 2%, 3%, 4%, 5%, 10%, 20%, 30%, and 40% strain under five cycles applied under each strain level. A 10 s pause was applied at the peak amplitude of the third cycle under each strain level to allow an investigation of the signal-to-noise ratio (SNR). Capacitance data was recorded at 100 Hz using an inductance (L), capacitance (C), and resistance (R) - LCRmeter (Keysight E4980A), and the sensor's surface/apparent color under normal white light was simultaneously recorded using a digital camera with a frame rate of 30 fps during the cyclic loading process.

To allow a direct investigation of the mechanical properties of the structural color film, three of these films were customized to the same size and the mechanical properties were characterized by following the same experimental procedure. The color reflectance of the structural color film under different strain levels was measured using an optical fiber setup connected to an Ocean Optics HR2000+ spectrometer, and the measurements were carried out both before and immediately after film straining.

3.2. Fatigue crack test

The performance of the sensor at detecting and quantifying fatigue cracks was examined on C(T) specimens. The experimental test was conducted by following the same procedure as in prior work [31]. Figure 2(d) shows the overall experimental setup. The C(T) specimens were fabricated from A36 structural steel plates and machined using water-jet cutting to adopt the configuration prescribed by ASTM E647-15a [32], as presented in figure 2(c).

The C(T) specimens were prepared by successively sanding with 1000 grit sandpaper and rinsing the surface with isopropyl alcohol to provide a smooth and clean sensing area for the sensor. The sensor was fully adhered onto the front surface of the C(T) using a thin layer of off-the-shelf bi-component epoxy resin (JB Weld), and a peel-and-stick tape measure was adhered onto the back surface of the C(T) specimen to visualize and quantify the crack length using photographs taken during the test. The front and back views of the sensor-C(T) specimen are respectively shown in figures 2(e) and (f). A pair of clevises was used to mount the sensor-C(T) specimen on the 647 hydraulic wedge grip, and a closed-loop servo-hydraulic testing machine (MTS model 312.41 with a TestStar IIm controller) was used to apply fatigue load. Washers were used in conjunction with screw nuts to prevent relative sliding and stress concentration. Two mobile phone cameras (A and B) were placed on the back and front sides of the sensor-C(T) specimen to simultaneously record the crack length and sensor's color during the loading process at frame rates both of 30 fps.

To focus on the sensor's performance in detecting low-cycle fatigue cracks and quantifying different levels of damage, a 1 Hz harmonic excitation was applied to the sensor-C(T) specimen, and the loading range was assigned in the tension-tension mode with a constant loading range from 2.9 kN (0.65 kips) to 29 kN (6.5 kips), resulting in a constant stress intensity ratio R of 0.1, to generate and extend a fatigue crack. Note that this loading resulted in a stress intensity higher than that prescribed in ASTM E647-15am [32], which facilitated a more rapid crack growth in this study. Values of Paris' coefficients $C_1 = 3.22 \times 10^{-10}$, $C_2 = 3.19 \times 10^{-10}$ (m/cycle), and $m_1 = 2.87$, $m_2 = 2.86$ were respectively found on specimens 1 and 2, consistent with the valid ranges reported in literature [33, 34].

Load and displacement were recorded using the linear variable displacement transducer of the MTS with a sampling frequency of 20 sample s^{-1}, and capacitance data were collected at 10 samples s^{-1} using an LCR meter (Agilent 4263B)

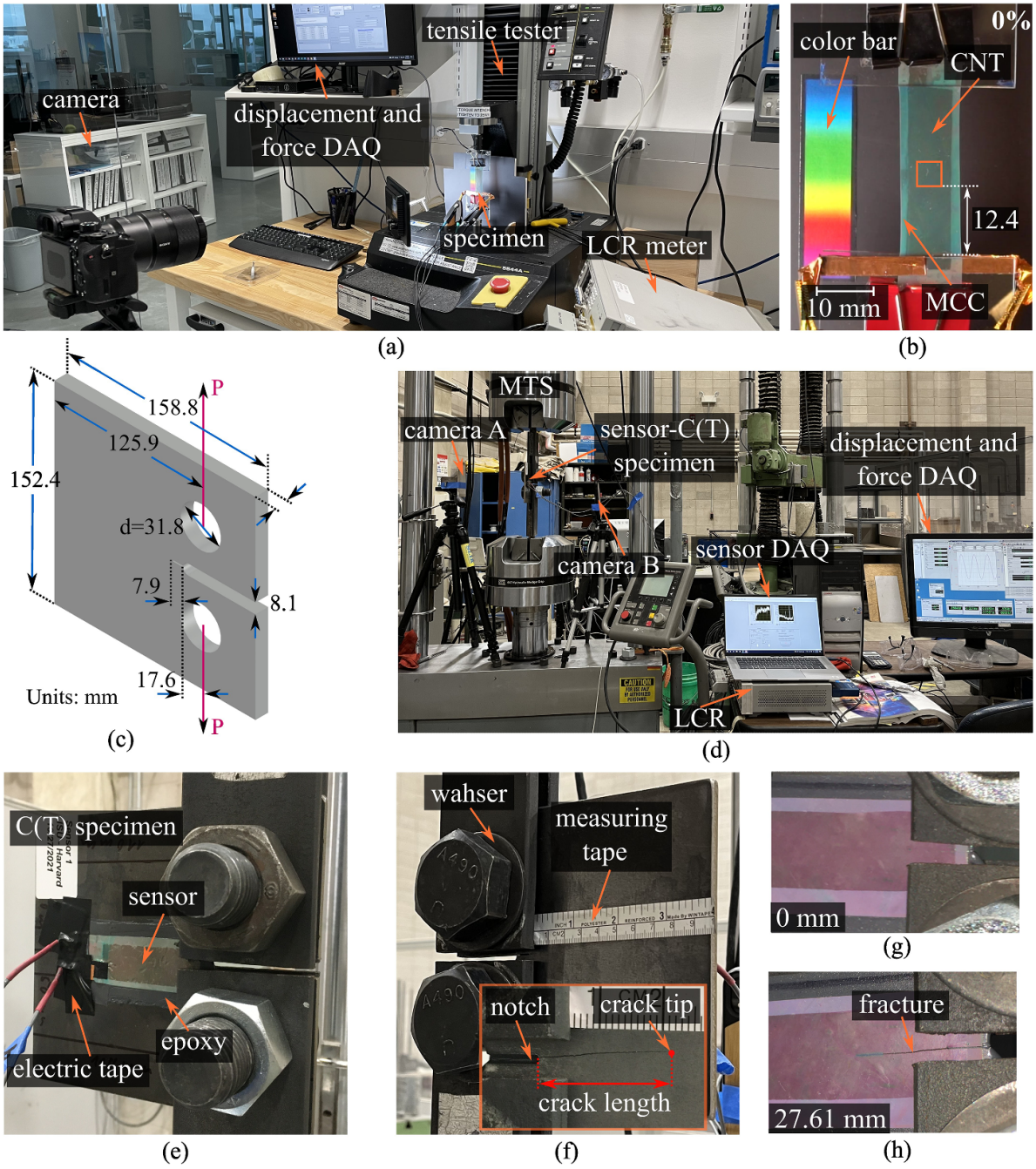

Figure 2. (a) Experimental setup of the free-standing test; (b) close-up view on the free-standing sensor (front view); (c) geometry of the C(T) specimen; (d) overall experimental setup for fatigue crack test; (e) close-up view of the front surface of the sensor-C(T) specimen; (f) close-up view of the back surface of the sensor-C(T) specimen; (g) picture of the sensor under 0 mm crack length; and (h) picture of the sensor under 27.61 mm crack length.

at a 1 kHz measuring frequency driven in LabVIEW environment. Wires were fixed with electrical tape to create an electrically insulating barrier and minimize the electrical noise caused by cable movement. In this study, crack length was defined as the distance measured from the notched edge to the crack tip (indicated as a red dot in figure 2(f), where a fatigue crack of 20.1 mm was observed taken at cycle 13 059). Tests ran continuously until the maximum displacement of the MTS machine reached 25.4 mm (1 inch). Slight lateral torsion-induced out-of-plane deformations were observed on the C(T) specimen for crack lengths beyond 38.1 mm.

4. Sensor characterization

This section presents and discusses the experimental results obtained from the free-standing tests. First, the mechanical properties of the structural color film are presented. Second,

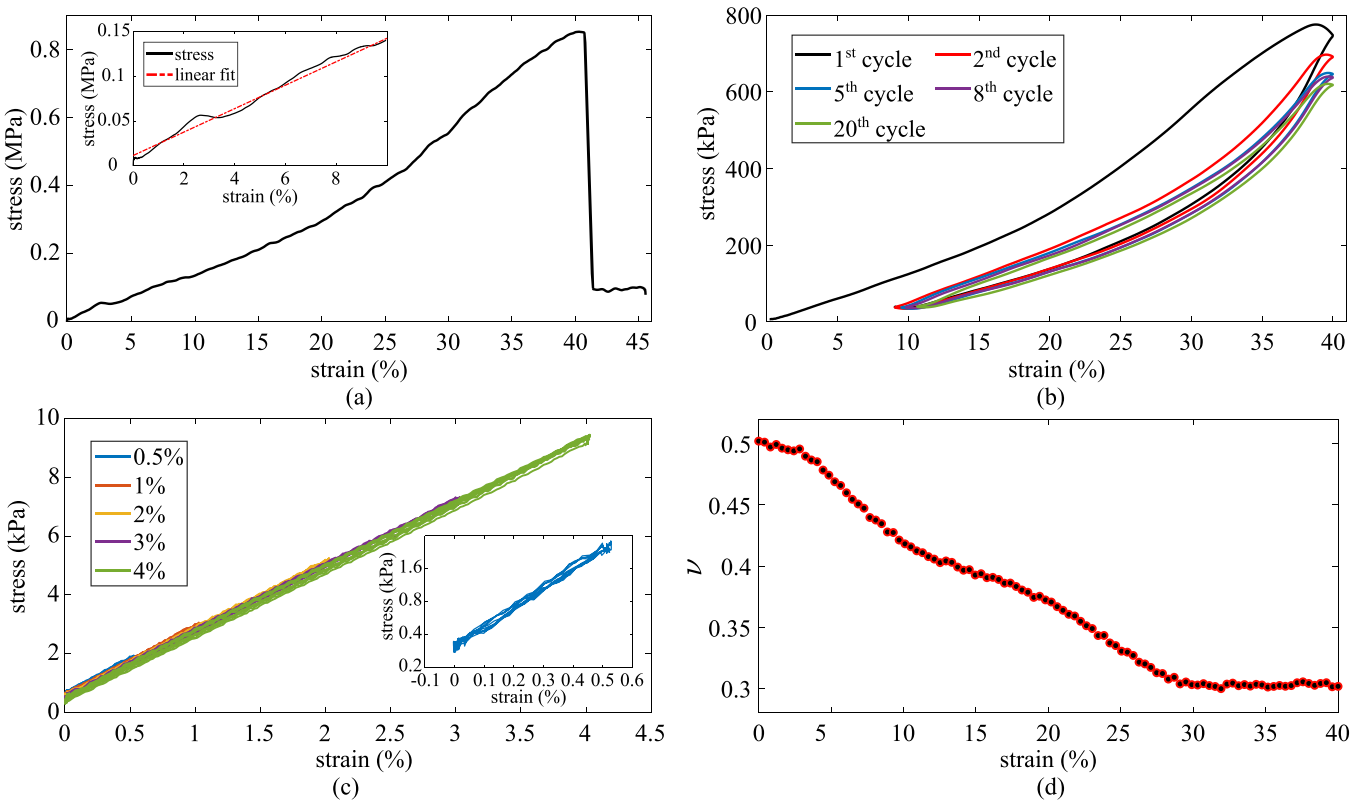

Figure 3. (a) Stress–strain curve of the structural color film taken from the tensile rupture test with the inset showing the linear fit over 10% strain; (b) comparison of the stress–strain response of the structural color film under the 1st, 2nd, 5th, 7th, and 20th cycle; (c) cyclic stress–strain curve of the multifunctional sensor under 0.5%, 1%, 2%, 3%, and 4% strain with inset showing the showing the stress–strain behavior and hysteresis loop within 0.5% strain; and (d) strain-dependent Poisson's ratio of the mltifunctional sensor measured using ImageJ.

the optical properties of the structural color film in terms of the apparent color, color change, and reflectance under different strain levels are presented. Third, the electrical properties of the sensor under quasi-static excitations are characterized and evaluated.

4.1. Mechanical properties

Figure 3(a) shows the stress–strain curve obtained from the tensile rupture test conducted on the structural color film. The material exhibited a linear stress–strain relationship before the brittle fracture, and a significant drop in stress was observed after the strain reached 42.1%, associated with a creep rupture of the material. A Young's Modulus $E = 0.46$ MPa was found from the elastic region (top-left inset of figure 3(c)) and determined from the slope of the linear fit, and an ultimate strength of 0.87 MPa was computed from the maximum load before the final rupture/fracture. This strength capacity is well beyond what would be required to sustain local deformations from a fatigue crack located under the sensor [12].

Figure 3(b) presents a set of cyclic stress–strain experiments of the color film exposed to 40% strain. A noticeable vertical downward shift was observed on the curve after the 1st cycle. The hysteresis loss after the first cycles under the cyclic loading and unloading process can be explained by the Mullins effect and stress softening induced by the rearrangement and breaking down of the polymer chains under stretch, and has been reported as a common phenomenon that occurs within elastomeric materials [35]. Our experiments show that the cyclic behavior exhibits a stable status through a rapid recovery to the equilibrium status after the 2nd cycle, displaying a hyperelastic stress–strain response typical of elastomers. The toughnesses of the elastomeric composites were determined using the enclosed area below each stress–strain curve, and the high durability and robustness of the material were found to be fully preserved even after subjecting to over 20 loading cycles, demonstrating the repeatability in the mechanical response and also the potential for its application to cyclic loading scenarios.

Figure 3(c) is an overview of the cyclic stress–strain curve of the sensor under 0.5%, 1%, 2%, 3%, and 4% strain, with the inset showing the hysteresis loops at relatively lower strain amplitudes of 0.5%. It can be seen that at the area of hysteresis loops remained approximately the same and are narrow, indicating that the elastic strain is much higher than the plastic strain under small strain level.

Figure 3(d) shows the strain-dependent Poisson's ratio ν of a virgin sensor under increasing strain of the tensile rupture test. Results were obtained by measuring transverse shrinkage of the sensor through the image processing software ImageJ, and an overall decrease as a function of applied strain was observed until convergence at approximately 30% strain.

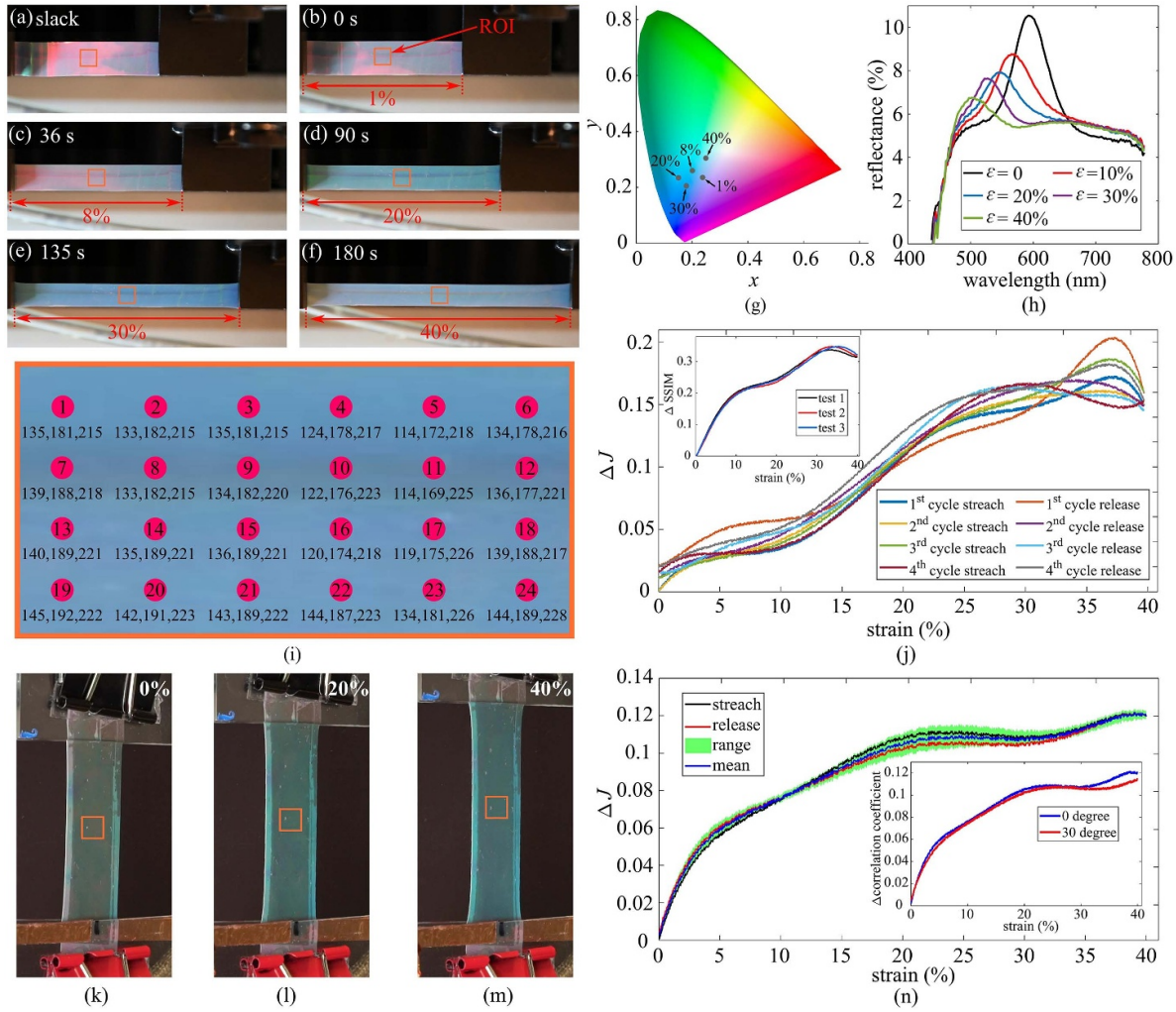

Figure 4. (a)–(f) Digital photos of the structural color film at 0%, 1%, 8%, 20%, 30%, and 40% strain under ambient condition; (g) measured reflectance spectra of the structural color film at different strain levels; (h) CIE 1931 color space chromaticity plotting the color change of structural color film at different strains; (i) 24 color points organized RGB matrix of the first frame (0% strain); (j) ΔJ as function of strain for the structural color film during the stretch and release processes of the first four cycles, with the inset showing the change in SSIM (Δ SSIM) in the defined ROI; (k)–(m) digital photos showing the apparent color of the sensor at (k) 0, (l) 20%, and (m) 40% strain; and (n) change in correlation (ΔJ) versus applied strain of the sensor during the stretch and release processes with the inset comparing the mean ΔJ curves computed from 0° and 30° measurements.

4.2. Optical properties

Figures 4(a)–(f) present images taken from the recorded experiment under ambient conditions (normal white light), showing the multifunctional sensor's apparent color at slack, and under 1%, 8%, 20%, 30%, and 40% strains, respectively. Here, the applied strains result in a remarkable and naked-eye observable color change from light blue to a deeper blue and finally to cold white.

The Commission Internationale de L'Éclairage's (CIE) coordinate system was used to define the color coordinates, and the calculated CIE 1931 color space chromaticity of the structural color film at different strain levels are plotted in figure 4(g). It can be observed that the coordinates change with increasing strain and is evident for optical strain sensing.

The light scattering behaviour of the multifunctional sensor at different strain levels are displayed in figure 4(h). A distinguishable peak in diffuse reflectance was observed at each stretch level, and all reflectance peaks are centered around the wavelength of approximately 500–650 nm, characteristic of the turquoise color. The measured wavelength of the peak intensity gradually decreased with the increase of strain, while the peak intensity in diffuse reflectance decreased 20.5% when stretching of the color film from 0% to 10% strain, indicating a higher optical sensing sensitivity over that strain range.

To investigated the reversibility of the color changes during the loading and unloading cycle, an 8 mm × 8 mm square-shaped region at the center of the sensor, where the axial deformation is the most uniform and the observed color change is the most homogeneous, was defined as a region of interest (ROI), identified by the orange box in figures 4(a)–(f). The 8 mm length selected here corresponds to a 14.28% gauge length, achieving an ROI with dimensions comparable

with the width of the sensor. After, 24 color points were uniformly assigned on the defined ROI, indicated as red dots in figure 4(i), to identify the red, green and blue (RGB) value on that location and formed as an RGB color matrix, as presented in figure 4(i).

The Pearson correlation coefficient J, which is computed as the ratio between the covariance of two RGB color matrices and the product of their standard deviations, was adopted as the color change indicator to measure the linear correlation between the surface color that appeared on each frame, written as:

$$J = 1 - \frac{\mathbb{E}\left[\left(S_{i,k} - \mu_s\right)\right]\left[\left(S^0_{i,j} - \mu_{S^0}\right)\right]}{\sigma_s \sigma_{s^0}} = 1 - \frac{\sum_{i,k}\left(S_{i,k} - \mu_s\right)\left(S^0_{i,j} - \mu_{S^0}\right)}{\sqrt{\sum_{i=1}^{n}\left(S_{i,k} - \mu_s\right)^2}\sqrt{\sum_{i=1}^{n}\left(S^0_{i,j} - \mu_{S^0}\right)^2}} \quad (13)$$

where $S_{i,j}$ and $S^0_{i,j}$ are the RGB matrices of the first frame and the compared frame, $\mathbb{E}$ is the expected value, μ_S and μ_{S^0} are the means of $S_{i,j}$ and $S^0_{i,j}$, and σ_s and σ_{s^0} are their standard deviations, respectively.

The results of the change in correlation coefficients (ΔJ) during the stretch and release processes of the first four cycles are presented in figure 4(j). A non-linearity after 30% strain can be observed, which can be explained by the edge effects. Additionally, the highest value for ΔJ was obtained between approximately 40%–30% strain during the strain release phase of the first cycle, indicating a path-dependant color change after the first cycle of stretching. A positive and approximately linear relationship was observed between the change in correlation coefficients and the applied strain, and an optical gauge factor of 0.53 was found from the slope of the linear regression conducted in the 0%–30% strain range.

The defined ROI was used for cropping and extracting images used for color change analysis. The plot of the computed change in SSIM (Δ SSIM) between the first frame and each other frames is shown in the inset of figure 4(j). Results in the plot are taken from the stretch during the second cycle of three tests conducted on three independent specimens. The overlap and close agreement between the experimental data measured from three independent specimens were evaluated by comparing the area below each SSIM curve that resulted from the stretch and release process. The enclosed area remained in the range of 6.11–6.29 during the stretch and release process, illustrating the repeatability of the color change on the structural color film. A similar underlying trend between the RGB correlation loss and the computed SSIM was observed, evident in the strain-induced color change on optical response.

Figure 2(b) is a digital photo taken from the front view (0°) showing the surface color of the free-standing sensor under 0% strain. An 8 mm × 8 mm ROI with 24 color is also assigned for creating RGB matrices. Results for ΔJ taken from the stretch and release process during the first cycle are presented in figure 4(n) as a function of strain, with the green area illustrating the range measured over ten cycles and with the blue curve representing the mean value. To illustrate the angle independence of the strain-depended color change, the experiment was recorded under an angle of 30° normal to the sensor. Figures 4(k)–(m) are digital images taken from that angle, showing the color of the free-standing sensor under 0%, 20%, and 40% strain. Results from the mean ΔJ curve was compared against those measured from front view (0°) and presented in the inset of figure 4(m). An root mean square error (RMSE) value of 2.39% was found over 0%–30% strain, demonstrating an angle-independent color change.

4.3. Electromechanical properties

The sensing performance of the sensor was investigated by evaluating the signal's linearity, gauge factor, capacitance versus strain match, and resolution. Figure 5(a) presents a time series plot of the relative change in capacitance $\Delta C/C_0$ versus applied strain at a rate of 1% s^{-1}. Results exhibit excellent linearity up to 35%, and a RMSE of 97.36% over the full 40% strain range, and the gauge factor obtained using the linear fit over the 10% strain range (inset of figure 5(a)) is $\lambda = 0.49$, taken as the slope of the fit. Figure 5(b) presents the strain accuracy $e_1(\pm 0.18\ \varepsilon)$ and capacitance error bounds $e_2(\pm 0.05\ \Delta C/C_0)$, both computed from the linear fit over 10% strain.

Figure 5(c) plots the relative change in capacitance $\Delta C/C_0$ compared against the strain input under cyclic loading with the strain level successively increasing to 0.5%, 1%, 2%, 3%, 5% and up to 40%. Results show an good agreement between both signals, with an RMSE of 3.88% and an overall SNR value of 10.62 dB, indicating the strain tracking capability and the high quality in signal. The 95% confidence interval (CI) bound in terms of strain and relative change in capacitance yields an accuracy of $\pm 0.65\,\mu\varepsilon$ and $\pm 0.29\ \Delta C/C_0$.

5. Fatigue crack monitoring

This section presents and discusses experimental data obtained from the fatigue crack test to validate the capability of the sensor at optically and electromechanically detecting and characterizing fatigue cracks. First, the optical sensing performance for fatigue crack localization is illustrated. Second, the electromechanical sensing performance in terms of linearity, sensitivity, resolution, and accuracy are evaluated. Third, the results obtained from optical sensing are compared with the results from electrical sensing for quantifying a crack.

5.1. Optical sensing

Figures 6(a)–(c) presents digital photos taken from the video recorded continuously during the fatigue tests. Selected photographs show that the color changes on the sensor under a large opening, no opening, and a small opening for a crack length of 16.3 mm taken at 10 361 cycles. A color change of the sensing area above the cracking area was observed under the cross-crack strain provoked by the opening of the crack. The digital photos are further processed with CIELAB-based color-difference formulas (CIE 2000) in MATLAB to

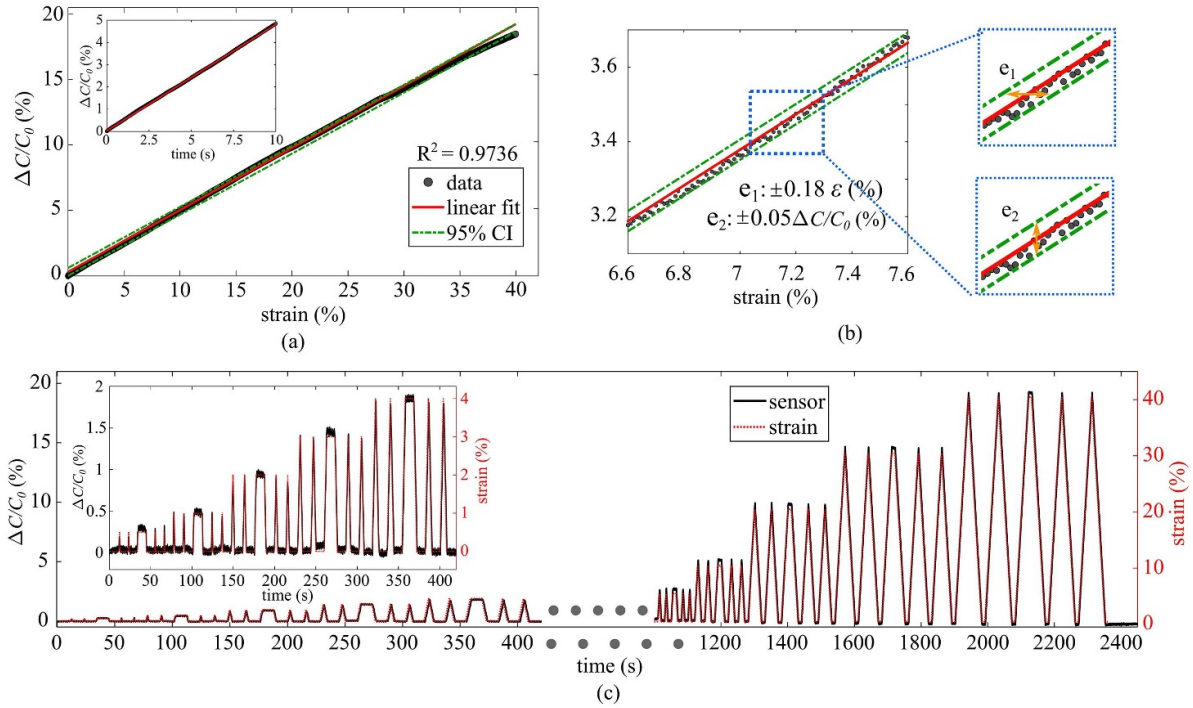

Figure 5. (a) Quasi-static tensile test results over 40% strain level; (b) strain accuracy resulted from the capacitance error bounds; and (c) time series response of the sensor under cyclic loading (superimposed).

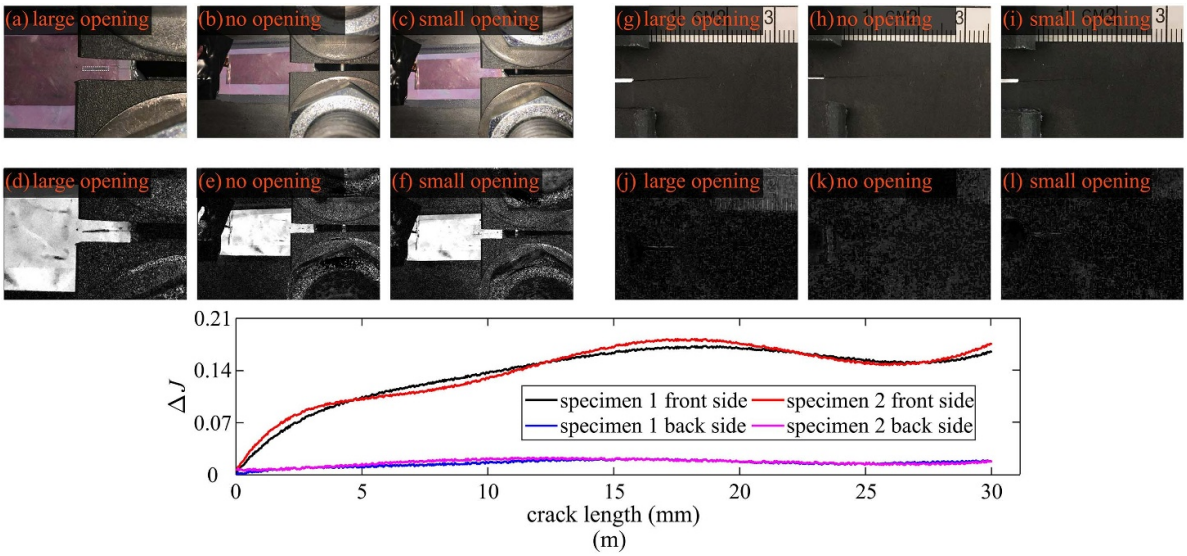

Figure 6. (a)–(c) Digital photographs of the sensor under a crack length of 16.3 mm (at 10 361 cycles): large crack opening, no crack opening, and small crack opening; (d)–(f) CIE 2000 processed images of digital photographs (a)–(c); (g)–(i) digital photographs from the back surface of the C(T) under a crack length of 16.3 mm (at 10 361 cycles): large crack opening, no crack opening, and small crack opening; (j)–(l) CIE 2000 processed images of digital photographs (g)–(i); and (m) comparison of the change in correlation (ΔJ) computed from the front side (sensor) and back side (no sensor) of the C(T) specimen.

improve the accuracy of observed color differences through the introduction of various corrections in CIELAB. Results of the processed photographs are shown in figures 6(d)–(f). Differences in the sensor's apparent color can be observed even under a small crack opening. Figures 6(g)–(i) are images taken from the back side of the C(T) specimen that correspond to figures 6(a)–(c), emulating pictures that would be taken during a traditional inspection. Those photographs are also processed with the CIE 2000 coordinate, and the resulting photographs are shown in figures 6(j)–(l). By comparing the processed photographs of the sensor (figures 6(d)–(f)) and the back side of the C(T) specimen (figures 6(j)–(l)), it can be noticed that the sensor improved visual capabilities to observe a fatigue crack. Figure 6(m) is a plot comparing ΔJ taken over the front side (sensor) and back side (no sensor) specimen, for both tested specimens. Results clearly show that the utilization

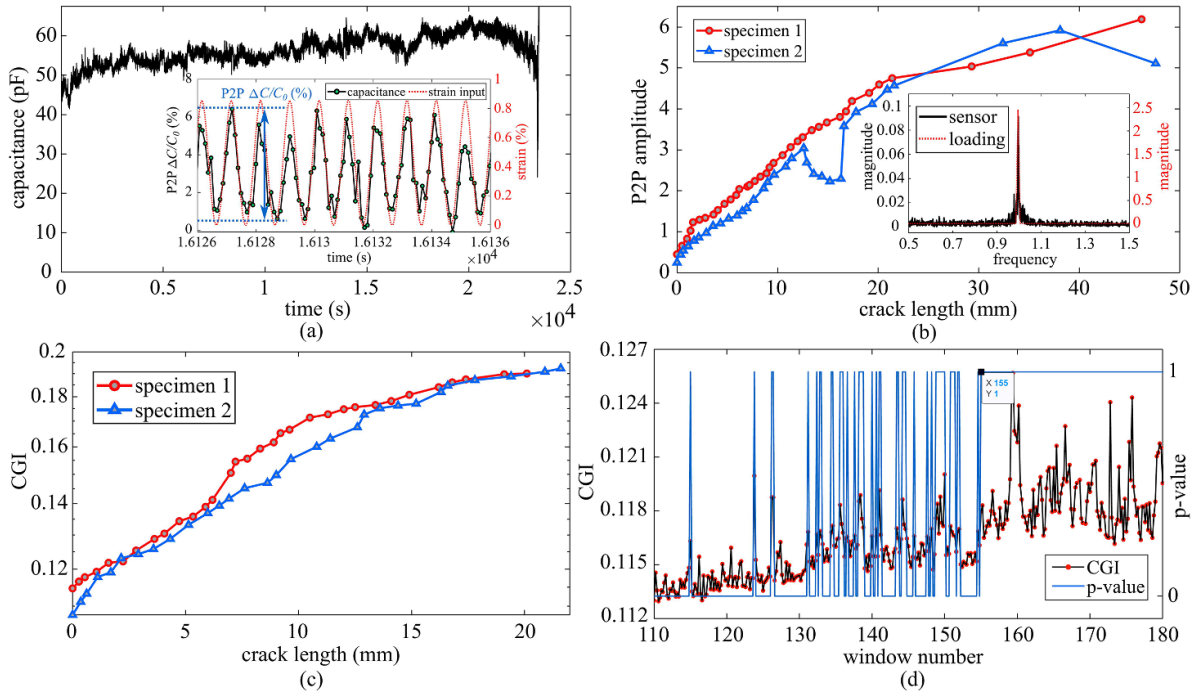

Figure 7. (a) Time series of raw capacitance data under designed fatigue loading protocol; (b) P2P amplitudes of the relative change in capacitance $\Delta C/C_0$ under different crack lengths, with the inset showing the frequency spectra of the sensor and the loading; (c) CGI as a function of crack length; and (d) time series of averaged CGI values along with corresponding p-values from the t-test.

of the sensor permits a better optical discovery of a fatigue crack, as well as a better characterization of the fatigue crack length.

5.2. Electromechanical sensing

Figure 7(a) plots a capacitance time history across the entire loading/unloading process, and the inset presented capacitance versus strain input under a crack length of 30.6 mm. The upward drift is capacitance data can explained by the plastic deformation of the C(T) specimen, where the minimum crack opening increased as the crack propagates. A peak-to-peak (P2P) relative change in capacitance $\Delta C/C_0$ amplitude (illustrated in the inset of figure 7(a)) was extracted as a signal feature to quantify the localized strain provoked by the closing and opening of the crack, which corresponds to the actual strain experienced by the sensor. This strategy allows to correct for drifts caused by calibration and in-field environmental effects. Note that the long-term performance of the device with respect to environmental effects is left to future work.

Figure 7(b) presents the P2P amplitudes extracted from both tested specimens over different crack lengths, where the P2P amplitudes are taken as the averaged values of 100 s measurements under a given crack length. An overall increase in P2P amplitudes is observed with the increase of the crack length. The increments of the P2P amplitudes under a unit crack length decreased after approximately 20 mm crack length, which can be attributed to the potential delamination of the sensor and rupture of the sensing area during the experiment, as shown in the figure 2(h), taken under a crack length of 27.61 mm. The inset of figure 7(b) compares the frequency spectrum of the sensor's signal and MTS inputs (i.e. force input), where the input frequency of 1 Hz is observable.

The crack length quantification was conducted by using the crack growth index (CGI) algorithm proposed in previous work [36]. Briefly, the CGI consists of a scalar that relates linearly to a fatigue crack size. It is taken as the square root of the ratio of the magnitude of the peak power spectral density of the capacitance signal (PSD_i^C) to the magnitude of the PSD of the force measurements (PSD_i^F), with $\mathrm{CGI} = \frac{\sqrt{\mathrm{PSD}_i^C}}{\sqrt{\mathrm{PSD}_i^F}}$. Figure 7(c) plots the computed CGI as a function of crack length in a semi-log scale plot, and linearity of the relationship was observed between 0 (no crack) to approximately 20 mm crack length.

A continuous t-test on the sensor's signal is used to determine the smallest detectable crack size from the signal. To do so, the CGI data was split into 25 s windows, and the 5th window (corresponding to the time interval 100–125 s) was taken as the reference window to reduce noise. Then, the t-test was conducted by using the TTEST function in MATLAB and under the null hypothesis that the new CGI values were different from the CGI values in the reference window. Figure 7(d) is a time series plot of the resulting p-value. A p-value of 1 indicates that the t-test rejects the null hypothesis at a 5% significance level, and thus that a crack is discovered. In this study, the p-values from specimens 1 and 2 stabilized to 1 after the 155th and 148th windows, respectively. Those windows correspond to time intervals of 3875 s–3900 s and 3700 s–3725 s, indicating minimum detectable crack lengths of 0.86 and 0.82 mm, respectively.

Figures 8(a)–(d) plot the averaged relative change in capacitance $\Delta C/C_0$ from both specimens as a function of the

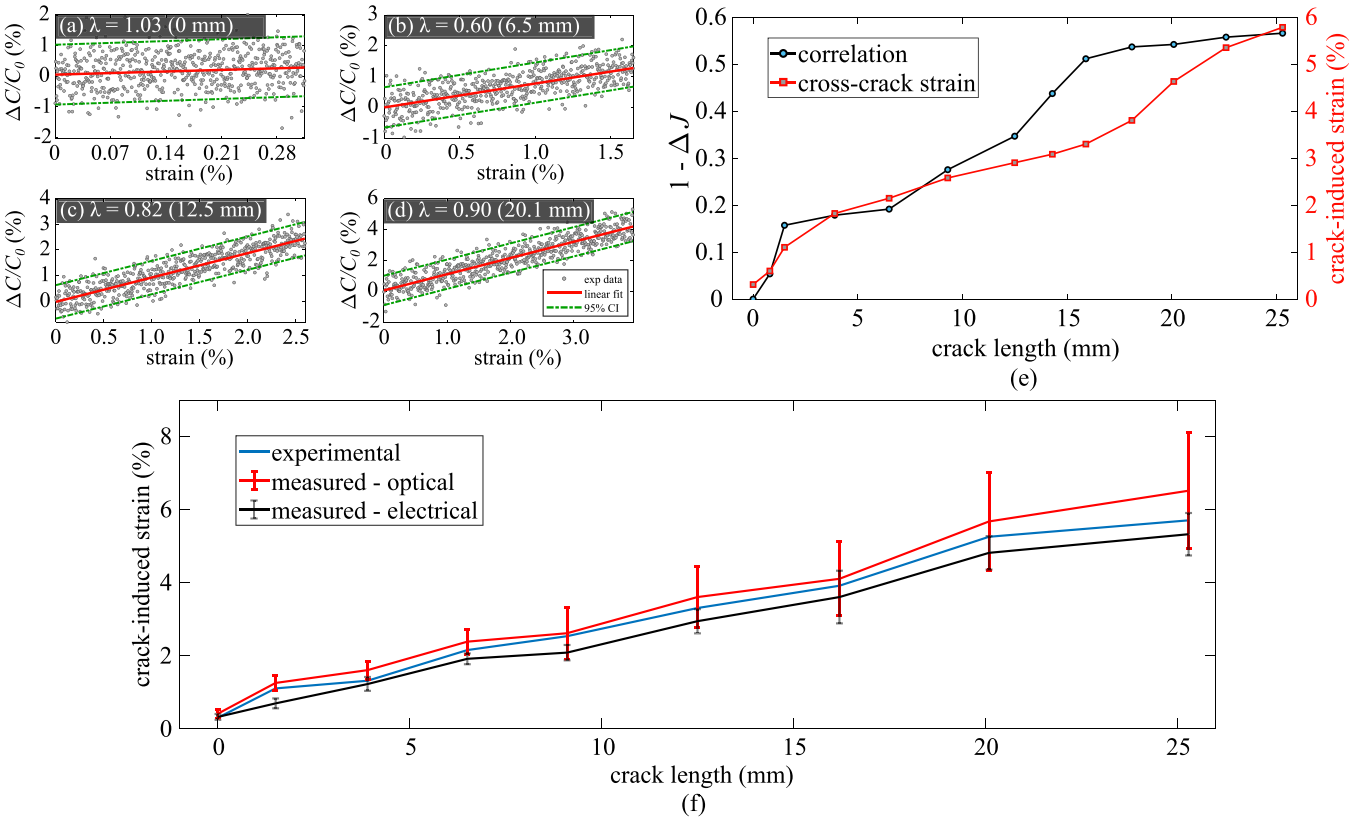

Figure 8. (a)–(d) Two sample-averaged relative change in capacitance ($\Delta C/C_0$) as a function of cross-crack strain under crack lengths of (a) 0, (b) 6.2, (c) 12.5, and (d) 20.1 mm, also presenting the gauge factors and signal matching error for with 95% CI; (e) correlation coefficients (black solid line) between the 20 color patches organized RGB matrices resulted from the cracking and noncracking area, along with the corresponding cross-crack strain levels (red dot line) under different crack lengths; (f) comparing of cross-crack strain measured from numerical model, optical sensing, and capacitance sensing under different crack lengths.

Table 1. Experimental results characterizing fatigue crack sensing performance.

Crack length (mm)	MTS strain (%)	Crack strain (%)	Strain ratio (%)	R^2 (−)	MTS λ (−)	Crack λ (−)	95% CI $\Delta C/C_0$ (−)	95% CI resolution ($\mu\varepsilon$)	σ_{res} (−)
0	0.39	0.31	125.81	0.19	0.82	1.03	±1.072	±90.8	30.12
1.5	0.43	1.11	37.74	0.23	1.59	0.62	±1.101	±69.2	26.71
6.5	0.56	2.16	25.93	0.46	2.32	0.60	±1.051	±45.3	22.98
12.5	0.79	3.31	27.01	0.52	3.03	0.72	±0.953	±31.4	24.43
20.1	0.88	5.26	18.96	0.64	4.77	0.79	±1.166	±27.4	20.77
29.3	0.97	6.44	15.06	0.87	5.05	0.76	±1.315	±26.0	19.29
35.1	1.16	8.39	13.83	0.95	4.48	0.62	±1.131	±28.2	21.38
41.9	1.41	10.56	13.35	0.91	3.78	0.50	±1.005	±26.6	18.61
47.6	1.62	13.11	12.36	0.93	3.15	0.39	±0.961	±30.5	19.09

crack-induced strain under crack lengths of 0, 6.2, 12.5, and 20.1 mm. The crack-induced strain is the localized strain provoked by the closing and opening of the crack, and is a better representation of the strain experienced by the sensor. These values are computed from a finite element model (FEM) under the corresponding crack lengths. The FEM for such test configuration was presented and validated in prior work [31]. Results show the linear fit (red solid line) obtained from least squares regression along with the resulting 95% CI bounds (green dashed line) representing the resolution. The computed gauge factors λ are listed in each subfigure.

Table 1 assembles the quantitative results over nine representative crack lengths, listing the load-derived strain from the MTS machine (MTS-strain), crack-induced strain, MTS-derived to crack-induced strain ratio, linearity through the quality of the linear regression fit (R^2), gauge factors (λ) computed from MTS-derived strain and crack-induced strain, resolution through the 95% CI in terms of the relative change

Table 2. Comparison of sensing performance versus cSEC under 0, 11.1, and 48.2 mm crack lengths.

	Crack length (mm)	multif. (sensor)	cSEC
R^2	0	0.19	0.17
(–)	11.1	0.51	0.83
	48.2	0.93	0.97
95% CI	0	±1.07	±0.59
$\Delta C/C_0$	11.1	±0.94	±0.29
(–)	48.2	±0.96	±0.23
95% CI	0	±90.8	±71.9
resolution	11.1	±32.6	±49.2
($\mu\varepsilon$)	48.2	±30.3	±12.2
σ_{res}	0	30.12	25.64
($\mu\varepsilon$)	11.1	23.39	4.78
	48.2	18.52	2.77
min. crack length (mm)	—	0.84	0.28

in capacitance and equivalent strain levels computed using equation (7) with MTS-induced λ, and standard derivation on the resolution (σ_{res}) measured from specimens 1 and 2. Results show that both the MTS-derived strain and crack-induced strain are increasing with the extension of the crack length, but with the crack-induced strain increasing at a higher rate, resulting in a decrease of the strain ratio as the crack propagates. Values for R^2 and the crack-induced λ respectively exhibit an overall good linearity and sensitivity, especially under a large strain. Yet, a relatively poor linearity was observed under the 0 mm crack ('no crack'), given the nonexistent crack-induced strain. The slightly lower crack-induced λ under large crack lengths (41.9 and 47.6 mm) can be attributed to the loss in the geometric sensing area. The resolution of the signal and accuracy (σ_{res}) improved with the increase in crack length, where the accuracy is computed as the standard deviation of data under a given crack length.

The performance of the multifunctional sensor is compared against that of a more mature parallel-plate capacitor (termed corrugated soft elastomeric capacitor or cSEC) reported in prior work on the exact same experimental setup [31]. Results are tabulated in table 2. It found that generally, the multifunctional sensor underperforms the cSEC probably due to its early stage of development. Yet, the reported values remain similar to those reported under the cSEC, except for the variance of the resolution, where the multifunctional sensor underperforms by one magnitude.

The optical strain sensing properties of the sensor is evaluated on an $l \times w = 5 \times 1\ \text{mm}^2$ rectangular ROI located above the crack with 20 color points uniformly assigned within the region. The loss in correlation coefficients ($1 - \Delta J$) between the RGB matrices that are computed under different crack lengths are presented in figure 8(e). It can be observed that the loss in correlations increases following a trend similar as a function of crack length to that of the crack-induced strain, consistent with the findings from the tensile tests conducted on the structural color film. This illustrates the capability of the sensor at optically localizing and quantifying crack.

Figure 8(f) is a plot comparing the crack-induced strain extracted from the numerical model using experimental data with measurements obtained from the optical and electrical (capacitance) signals. Values are presented as the average from both specimens. The optical-derived values were computed using the curves in figure 4(n), and the electrical-derived values were computed using the gauge factor λ characterized from prior tensile test. The error bars added to the optical measurements show the strain resolutions and the error bars added on the electrical-derived values indicate the min–max range over both specimens. Both optical and electrical sensing capabilities agree with the experimental data, with the optical response slightly overestimating crack-induced strain while the electrical feedback slightly underestimates it.

6. Conclusion

This paper presented a first study on a new multifunctional sensor that combines optical and electrical sensing properties. The device is a parallel plate capacitor fabricated by sandwiching a structural color film between transparent electrodes. The structural color film is fabricated by dispersing silica nanoparticles within a polymer matrix to produce an angle-independent color change. A stamp filtration step is used to apply the compliant CNT electrodes and fabricate the capacitor structure. One role of the optical response is to assist inspections, while one role of the electrical feedback is to send advance warnings of possible damage.

Free-standing and fatigue crack tests were performed to investigate and characterize the sensor. Stress–strain response and stress softening properties under cyclic loadings were characterized, and the reflectance spectra within the visible spectrum measured. An RGB color points-based algorithm was used as targets to quantify color change and evaluate the optical sensing performance as a function of strain. The electrical sensing performance was then evaluated under a free-standing configuration, and sensors were installed onto compact tension (C(T)) steel specimens to conduct fatigue crack detection tests.

Results from the free-standing test showed that the structural color film exhibited a rapid stress recovery ability and a linear stress–strain response within a larger strain level (40%). The functionality of the proposed RGB correlations matrix yielded an optical gauge factor of 0.53 and quantified the SSIM. It was found that the SSIM returned similar values under both 0° and a 30° viewing angles, illustrating the angle-independent color change property of the sensor.

Results from the fatigue crack tests demonstrated the sensor's capability to detect and quantify cracks using color and capacitive changes over large areas. In particular, the color change, linearity, sensitivity, resolution, and accuracy of the sensor were investigated. The sensor exhibited distinct color changes at the location of the crack opening and, with color levels consistent with those obtained from the free-standing tests. The sensor's electrical properties yielded good performance that compared with a more mature capacitance-based sensing skin technology. In particular, an average minimum

detectable crack length of 0.84 mm was achieved with the electrical signal. Overall, the presented work showed the promise of the multifunctional sensor for SHM applications requiring the on-time identification of strain-induced damage. Critical applications other than fatigue cracks in steel include cracks in pre-stressed concrete components and in aircraft airframes.

Data availability statement

The data that support the findings of this study are available upon reasonable request from the authors.

Acknowledgments

The authors gratefully acknowledge the financial support of the Departments of Transportation of Iowa, Kansas, South Carolina, and North Carolina, through the Transportation Pooled Fund Study TPF-5(449), and of the National Science Foundation through the Harvard University Materials Research Science and Engineering Center DMR-2011754.

ORCID iDs

Han Liu https://orcid.org/0000-0003-3057-522X
Simon Laflamme https://orcid.org/0000-0002-0601-9664

References

[1] Haghani R, Al-Emrani M and Heshmati M 2012 Fatigue-prone details in steel bridges *Buildings* **2** 456–76
[2] Chowdhury P and Sehitoglu H 2016 Mechanisms of fatigue crack growth—a critical digest of theoretical developments *Fatigue Fract. Eng. Mater. Struct.* **39** 652–74
[3] Campbell L E, Connor R J, Whitehead J M and Washer G A 2020 Benchmark for evaluating performance in visual inspection of fatigue cracking in steel bridges *J. Bridge Eng.* **25** 04019115
[4] Zolfaghari A, Zolfaghari A and Kolahan F 2018 Reliability and sensitivity of magnetic particle nondestructive testing in detecting the surface cracks of welded components *Nondestruct. Test. Eval.* **33** 290–300
[5] Chen Z, Lu W, Chen Y and Lu C 2020 Fatigue crack detection in AISI 304 austenitic stainless steel using nonlinear and linear ultrasonic testing methods *J. Mater. Eng. Perform.* **29** 4040–6
[6] Hajshirmohammadi B and Khonsari M M 2020 A simple approach for predicting fatigue crack propagation rate based on thermography *Theor. Appl. Fract. Mech.* **107** 102534
[7] Kurnyta A, Kowalczyk K, Baran M, Dziendzikowski M and Dragan K 2021 The use of silver conductive paint for crack propagation sensor customization *2021 IEEE 8th Int. Workshop on Metrology for AeroSpace MetroAeroSpace* (IEEE) (https://doi.org/10.1109/MetroAeroSpace51421.2021.9511716)
[8] Lin Y-A, Zhao Y, Wang L, Park Y, Yeh Y-J, Chiang W-H and Loh K J 2020 Graphene k-tape meshes for densely distributed human motion monitoring *Adv. Mater. Technol.* **6** 2000861
[9] Gupta S, Lin Y-A, Lee H-J, Buscheck J, Wu R, Lynch J P, Garg N and Loh K J 2021 In situ crack mapping of large-scale self-sensing concrete pavements using electrical resistance tomography *Cem. Concr. Compos.* **122** 104154
[10] Aygun L E, Kumar V, Weaver C, Gerber M, Wagner S, Verma N, Glisic B and Sturm J C 2020 Large-area resistive strain sensing sheet for structural health monitoring *Sensors* **20** 1386
[11] Kong X, Li J, Collins W, Bennett C, Laflamme S and Jo H 2018 Sensing distortion-induced fatigue cracks in steel bridges with capacitive skin sensor arrays *Smart Mater. Struct.* **27** 115008
[12] Liu H, Laflamme S, Li J, Bennett C, Collins W N, Eisenmann D J, Downey A R J, Ziehl P and Jo H 2022 Investigation of textured sensing skin for monitoring fatigue cracks on fillet welds *Meas. Sci. Technol.* **33** 084001
[13] Sun J, Bhushan B and Tong J 2013 Structural coloration in nature *RSC Adv.* **3** 14862
[14] Behera A 2021 Chromogenic materials *Advanced Materials* (Cham: Springer) pp 157–91
[15] Yue Y and Gong J P 2015 Tunable one-dimensional photonic crystals from soft materials *J. Photochem. Photobiol.* C **23** 45–67
[16] Phillips K R, England G T, Sunny S, Shirman E, Shirman T, Vogel N and Aizenberg J 2016 A colloidoscope of colloid-based porous materials and their uses *Chem. Soc. Rev.* **45** 281–322
[17] Kim S-U, Lee Y-J, Liu J, Kim D S, Wang H and Yang S 2021 Broadband and pixelated camouflage in inflating chiral nematic liquid crystalline elastomers *Nat. Mater.* **21** 41–46
[18] Zeng S, Zhang D, Huang W, Wang Z, Freire S G, Yu X, Smith A T, Huang E Y, Nguon H and Sun L 2016 Bio-inspired sensitive and reversible mechanochromisms via strain-dependent cracks and folds *Nat. Commun.* **7** 11802
[19] Pulliam E, Hoover G and Ryu D 2017 Multifunctional mechano-luminescent-optoelectronic composites for self-powered strain sensing *ASME 2017 Conf. on Smart Materials, Adaptive Structures and Intelligent Systems* (https://doi.org/10.1115/SMASIS2017-3977)
[20] Ryu D, Loh K J, Ireland R, Karimzada M, Yaghmaie F and Gusman A M 2011 In situ reduction of gold nanoparticles in pdms matrices and applications for large strain sensing *Smart Struct. Syst.* **8** 471–86
[21] Fudouzi H, Sawada T, Tanaka Y, Ario I, Hyakutake T and Nishizaki I 2012 Smart photonic coating as a new visualization technique of strain deformation of metal plates *SPIE Proc.* **8345** 83451S
[22] Bae G, Seo M, Lee S, Bae D and Lee M 2021 Colorimetric detection of mechanical deformation in metals using thin-film mechanochromic sensor *Adv. Mater. Technol.* **6** 2100479
[23] Bae G, Seo M, Lee S, Bae D and Lee M 2021 Angle-insensitive fabry–perot mechanochromic sensor for real-time structural health monitoring *Adv. Mater. Technol.* **6** 2100118
[24] Grove T T, Masters M F and Miers R E 2005 Determining dielectric constants using a parallel plate capacitor *Am. J. Phys.* **73** 52–56
[25] Laflamme S, Saleem H S, Vasan B K, Geiger R L, Chen D, Kessler M R and Rajan K 2013 Soft elastomeric capacitor network for strain sensing over large surfaces *IEEE/ASME Trans. Mechatronics* **18** 1647–54
[26] Laflamme S, Ubertini F, Saleem H, D'Alessandro A, Downey A, Ceylan H and Materazzi A L 2015 Dynamic characterization of a soft elastomeric capacitor for structural health monitoring *J. Struct. Eng.* **141** 04014186
[27] Sara U, Akter M and Shorif Uddin M S 2019 Image quality assessment through FSIM, SSIM, MSE and PSNR—a comparative study *J. Comput. Commun.* **7** 8–18

[28] Peng J, Shi C, Laugeman E, Hu W, Zhang Z, Mutic S and Cai B 2020 Implementation of the structural SIMilarity (SSIM) index as a quantitative evaluation tool for dose distribution error detection *Med. Phys.* **47** 1907–19
[29] Brooks A C, Zhao X and Pappas T N 2008 Structural similarity quality metrics in a coding context: exploring the space of realistic distortions *IEEE Trans. Image Process.* **17** 1261–73
[30] Kumar R and Moyal V 2013 Visual image quality assessment technique using FSIM *Int. J. Comput. Appl. Technol. Res.* **2** 250–4
[31] Liu H, Laflamme S, Li J, Bennett C, Collins W, Downey A, Ziehl P and Jo H 2021 Investigation of surface textured sensing skin for fatigue crack localization and quantification *Smart Mater. Struct.* **30** 105030
[32] (ASTME647-15e1) 2015 Standard test method for measurement of fatigue crack growth rates *ASTM Int.* 1–49
[33] Ritchie R O 1999 Mechanisms of fatigue-crack propagation in ductile and brittle solids *Int. J. Fract.* **100** 55–83
[34] Pugno N, Ciavarella M, Cornetti P and Carpinteri A 2006 A generalized paris' law for fatigue crack growth *J. Mech. Phys. Solids* **54** 1333–49
[35] Cantournet S, Desmorat R and Besson J 2009 Mullins effect and cyclic stress softening of filled elastomers by internal sliding and friction thermodynamics model *Int. J. Solids Struct.* **46** 2255–64
[36] Kong X, Li J, Bennett C, Collins W, Laflamme S and Jo H 2019 Thin-film sensor for fatigue crack sensing and monitoring in steel bridges under varying crack propagation rates and random traffic loads *J. Aerosp. Eng.* **32** 04018116